12th International Symposium on Turbulence and Shear Flow Phenomena (TSFP12)
Osaka, Japan, July 19–22, 2022

AN EXPERIMENTAL STUDY OF PRESSURE DROP AND FLUID FLOW IN TRIPLY PERIODIC MINIMAL SURFACE (TPMS) SCAFFOLDS

Daejung Kim
Department of Mechnical Engineering
The University of Melbourne
Victoria 3010, Australia
daejungk@student.unimelb.edu.au

Chenxi Peng
Department of Civil and Infrastructure Engineering
RMIT University
Victoria 3000, Australia
S3756293@student.rmit.edu.au

Jonathan Tran
Department of Civil and Infrastructure Engineering
RMIT University
Victoria 3000, Australia
jonathan.tran@rmit.edu.au

Jimmy Philip
Department of Mechnical Engineering
The University of Melbourne
Victoria 3010, Australia
jimmyp@unimelb.edu.au

ABSTRACT

Cellular materials in nature have unique structures that show outstanding properties, which has led many scientists and engineers to manufacture them artificially. Among them, Triply-Periodic-Minimal-Surface (TPMS) scaffolds have drawn more attention due to their advantages over other similar lattice structures. With the development of the additive manufacturing known as a 3D-printing, many researchers have been manufacturing a variety of TPMS scaffolds with different methods, and then studing their mechanical behaviours. However, less attention is devoted to fluid dynamics in TPMS scaffolds. Here, to understand the flow behaviour in different TPMS scaffolds, measurements of pressure drop are carried out with two different structures, namely 'gyroid' and body-centered cubic (BCC), with three different porosities, and we compare the results with the classical Ergun equation used for flow through random sphere packing. The results from the gyroid scaffolds agree well with the Ergun equation within the laminar and the turbulent regimes once we introduce an equivalent hydraulic diameter. The results from the BCC scaffolds, however, deviate within the transitional and turbulent regimes. For further investigation, we select the highest porosity case of the BCC scaffolds and match its refractive index with the working fluid to conduct 2D-2C particle tracking velocimetry (PTV) measurements. We observe flow separation at nodes and recirculation flows between nodes at the different velocities demonstrating the dynamical changes with increasing Reynolds number.

Introduction

TPMS are surfaces generated by mathematical expressions that have zero mean curvature and three-dimensional (3D) periodicity. Due to these advantages, TPMS scaffolds have been of great interest to engineers and biologists. In structural engineering applications, TPMS scaffolds show outstanding mechanical properties compared to conventional lattice structures. Especially, TPMS scaffolds have high ratio of the surface to volume, which brings a lot of advantages in tissue engineering applications. For example, smooth and higher surface areas enhances cell adhesion, and open cell structures improve cell penetration and migration.

With the development of additive manufacturing, experimental studies on TPMS scaffolds have proliferated. This advanced technology has enabled the possibilities to customize pore size, morphology, and porosity that were the big obstacles encountered by traditional manufacturing processes. A variety of TPMS scaffolds are now manufactured with different materials, and their mechanical behaviours have been studied numerically and experimentally (e.g., Abueidda *et al.*, 2017). Also, some attention have been given to the permeability of TPMS scaffolds. Bobbert *et al.* (2017) and Castro *et al.* (2019) manufactured different TPMS scaffolds in a size of 15-20 mm and tested their permeability. They found that gyroid shows good permeability compared with other scaffolds, but due to the limited size of their specimen led to uncertainty in their conclusion, and the flow dynamics inside the scaffolds remains unknown. Furthermore, due to the primary focus on biomedical applications, the flow rates have been quite low; therefore, fluid behaviour at higher flow rates within these porous scaffolds has not been studied. This limits the application of TPMS scaffolds in other fields. As such, our broad aim is a comprehensive study of fluid behaviour in such complex internal architectures.

To achieve this, flow behaviours in different TPMS scaffolds are investigated experimentally. A gyroid is selected because of its complex internal architecture as a representative of TPMS scaffolds. Also, we choose a TPMS-based BCC scaffold due to its open cell structure. There are various ways to design TPMS topologies (Nitsche, 1989; Karcher, 1988; Brakke, 1992), but we adopt nodal surface approximations because of their mathematical expressions (Von Schnering & Nesper (1991)), which enables us to produce customized topologies using Matlab. In this method, either a solid or a sheet type of topologies are designed by choosing a level-set constant c (Al-Ketan & Abu Al-Rub (2019)). Since TPMS sheet scaffolds have large surface area that can be advantageous in many engineering applications, we design TPMS sheet gyroid (Vijayavenkataraman *et al.*, 2018; Al-Ketan & Abu Al-Rub, 2019) and BCC (Zhao *et al.* (2018)) in this study. The equations governing the TPMS geometry of 'gyroid' and

'BCC' are respectively given by:

$$u_{gyroid} \equiv cos(w_x x)sin(w_y y) + cos(w_y y)sin(w_z z) + cos(w_z z)sin(w_x x) - c = 0 \quad (1)$$

$$u_{BCC} \equiv cos(2w_x x) + cos(2w_y y) + cos(2w_z z) - 2(cos(w_x x)cos(w_y y) + cos(w_y y)cos(w_z z) + cos(w_z z)cos(w_x x) - c = 0 \quad (2)$$

Here x, y, and z are spatial coordinates in the three-dimensional Cartesian coordinate system, and w_x, w_y, and w_z are defined by $w_i = 2\pi\frac{n_i}{L_i}$ $(i = x, y, z)$. The constant value of c plays an important role to generate different thickness. Eq (1) and Eq (2) are solved using Matlab, and its built functions of isosurface and iscaps are used to generate desired surfaces of TPMS scaffolds. The $x-y$ view in figures 1(a) to (b) shows the geometry of gyroid and BCC respectively where its unit cell size is 12 mm×12 mm×12 mm. A 36 mm×36 mm×120 mm of gyroid and BCC respectively is produced in Matlab following the described procedure. This geometry is imported on Autodesk Netfabb software to make a cylindrical sample as shown in figure 1.

In the following sections, we will present a description of experimental set-ups for the measurements of pressure drop and particle tracking velocimetry. Then, the results of pressure drop measurements are compared with the Ergun equation (e.g., Ergun & Orning, 1949; Wood *et al.*, 2020).

$$\frac{3\Delta P}{2L}\frac{e^2 d_H}{\rho u_c^2} = 150\left(\frac{2}{3}\right)\frac{1}{Re_H/e} + 1.75, \quad (3)$$

where ΔP is pressure drop across length L of the scaffold, d_H is a hydraulic diameter, u_c is superficial velocity defined as the volumetric flow rate divided by the cross-sectional area of the tube where the scaffolds are placed, and e is porosity defined as the ratio of void volume to total volume.

The original Eq (3) is represented in terms of a pore diameter, but we replace it with a hydraulic diameter due to non-uniform pore sizes. We denote LHS of (3) as f_H, which is similar to the friction factor.

Experiments

A schematic of the experimental set-up for the pressure drops and 2D-PTV is shown in figure 2. For pressure drop measurements, the set-up consists of three main sections: the inlet, the measurement section, and the outlet. The inlet has a constant pressure head system, and a gravity driven flow is fed to the nozzle which includes honeycomb as flow straighteners. The fluid travels 1.3 m of acrylic tube with an inner diameter of 20.6 mm before entering the tube with scaffolds inserted, which covers a tube length of 1.53 m. The entrance length of 1.3 m is such that fully developed laminar flow enters the scaffold section. In the measurement section, a total length of 1.53 m of scaffolds at three different porosities ($e = 0.85$, 0.70, and 0.55) are inserted in separate acrylic tubes and connected to the inlet tube. For each tube, the first pressure tap is located 2 cm from the start of the scaffold section, the second tap is 75 cm from the first taps, and the last ones 75 cm from the second taps and 1 cm from the end of the scaffold section. Static pressures are measured using manometers at these three different locations. The manometers are carefully designed to minimize the effect of surface tension, and height measurements are carried out with sub-millimeter resolution. Water is used as the working liquid during pressure measurements. For the 2D-PTV, the same set-up is used as shown figure 2. The inlet section is maintained, and only the measurement section is replaced. The BCC scaffold at $e = 0.85$ is selected for velocity measurements. Spectra Physics EV 25 diode pumped solid state continuous 532 nm (green) laser is used to illuminate flow at 1 mm away from the center of the BCC scaffold. A PCO-dimax HS4 12 bit high speed camera with a resolution of 2000 × 2000 pixels is used in this experiment, which allows us to carry out time-resolved PTV measurements. We use (orange) fluorescent seeding particles combined with a green filter on the camera to block the reflection from scaffold geometry. To reduce optical distortions, a 59% of ammonium thiocyanate solution in water at 17°C is developed to match the refractive index (RI=1.48) of the BCC scaffold, and used as the working liquid. To reduce the refraction due to curvature of the tube, a 65 mm × 50 mm × 65 mm acrylic box filled with the working liquid is attached at the end of the 75 cm of the BCC scaffolds coinciding with the camera field-of-view (c.f.figure 2 inset: measurement 02).

Results

Figure 3(a) shows the result of pressure drop within the gyroid and BCC scaffolds measured across 1.5 m distance. Pressure drops are non-dimensionalized as shown on the left-hand-side of Eq (3). During the measurements, water is maintained at a temperature of 22°C resulting in constant viscosity and density. The net pressure drop is composed of viscous and pressure drag, each dominating respectively at lower and higher Re. At $Re_H/e < 100$, both the gyroid and the BCC scaffolds, although shifted along the ordinate, show a linear relationship that follow laminar drag law parallel to the Ergun equation represented in the solid line. In this case, gyroid with $e = 0.7$ and BCC scaffold with $e = 0.55$ show the closest trend to the Ergun values while maintaining the linear relationship, which suggests that theses geometries behave more or less similar to random packed spheres with similar pore diameters. The majority of the data, however, do not follow the Ergun equation. We, therefore, introduce the concept of 'an equivalent hydraulic diameter' d_{equ}. The essential idea is to find the equivalent hydraulic diameter that moves the laminar drag law region of each geometry to that given by the laminar region in the Ergun equation (for packed spheres). Thus, for each geometry, we are trying to find the equivalent sphere diameter that gives the same laminar viscous drag. To find the d_{equ} for gyroid and BCC, a slope in the region of the linear pressure drop is calculated by fitting the number of experimental data points in an increment of one data at each time. For example, the first and second data are fitted to find a slope and then by increasing one data point the first three data points are fitted to find a new slope. A next slope is calculated by fitting four data points.This process continues until a constant slope is no longer maintained. Taking the slope in the linear region, d_H is varied until a root mean square error (RMSE) between the laminar drag law and the experimental results become a minimum, that is less than 1% difference. The d_{equ} is thus defined as the final d_H obtained at the end of this procedure. All the data are replotted with d_{equ} and are shown in figure 3(b). Essentially, d_{equ} becomes a free parameter to make the laminar part of the normalised pressure drop data similar to that given by the Ergun equation. The results with the equivalent diameters of the gyroid scaffolds at the three different porosities agree well with the theoretical plot unlike that of the BCC

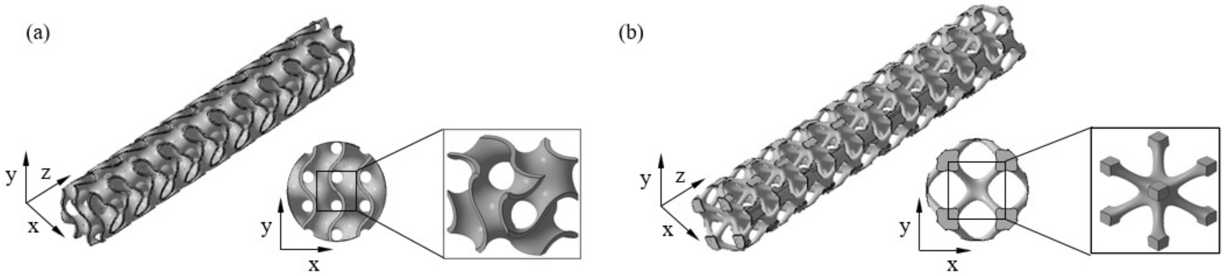

Figure 1. Isometric view of one sample of gyroid (a) and BCC (b) (d=20.54mm and L=120mm). One unit cell in 12 mm×12 mm×12 mm is in the middle highlighted in black rectangle in the $x-y$ view. In this design, one third of the one unit cell surrounds the one complete unit cell.

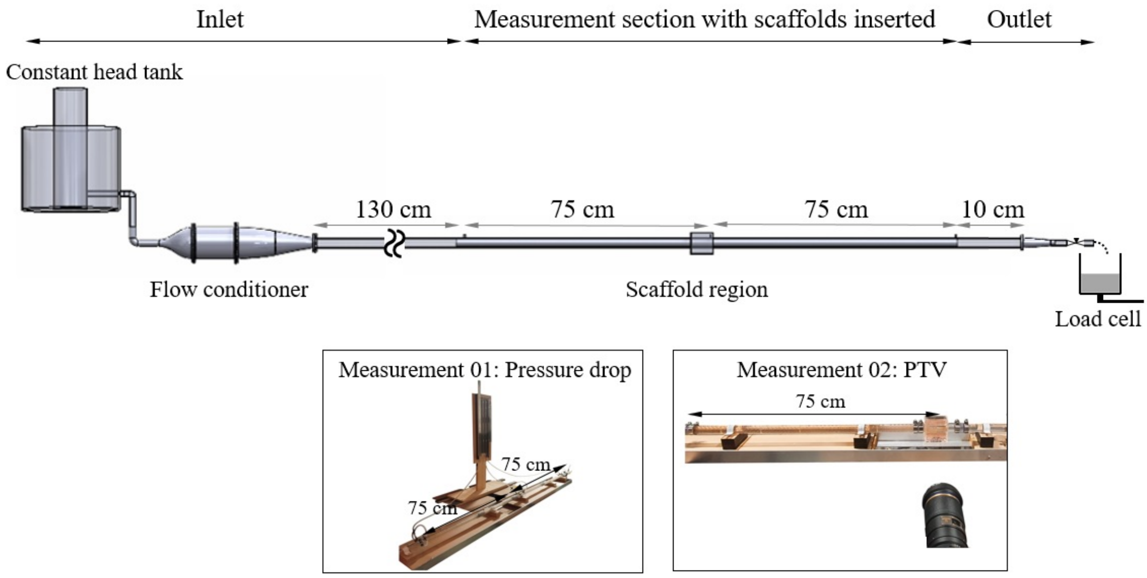

Figure 2. Experimental set-up schematic. Two different measurements are conducted, and a real picture of each measurement is shown in the measurement section. A needle valve controls flow rates at the outlet, and a load cell is used to calculate mass flow rates.

scaffolds. At $Re_H/e > 100$, the BCC scaffolds show different relationships, but having a similar pattern for the different porosities as the flow rates increase. These suggest the 'equivalence' of flow dynamics of the gyroid and random packed spheres because of the intricate geometrical structure of the gyroid. On the other hand, the open structure with sharper middle structure of the BCC scaffolds deviates from random spheres, which highlights the large-scale-inhomogeneities in the BCC scaffolds. To further understand the different behaviour of the BCC flow structure, velocity field corresponding to the highest Re=1500 for $e = 0.85$ in figure 4(a) is measured. Figures 4(a) to (c) show different views of the scaffold where velocity is measured. Figure 4(d), where several consecutive particle images are overlayed, shows flow recirculation in the pore regions between nodes. The recirculation region occurs owing to the relatively low velocities in the middle pore section compared to the high flows above and below the nodes as depicted in figure 4(e). Flow separation occurs at the beginning of the node, and backflow exists at the end of the node. The backflow is trapped in pore regions between two nodes due to the relatively high velocities passing above and below the nodes. Recirculation becomes stronger and chaotic as the flow rate increases. Such a flow behaviour is indeed different to what is expected from traditional porous media with random spheres.

Conclusion

The measurements of pressure drops in the gyroid and BCC scaffolds for three porosities are conducted. Non-dimensionalised pressure drops used to define an equivalent hydraulic diameter allows us to make direct comparison with the standard Ergun equation. This methodology for porous media is expected to be general, and has similarities to the concept of 'equivalent roughness height' widely used in rough-wall flows. Also, the velocity field of the BCC shows interesting results, which have not been reported in TPMS scaffolds. Due to the recirculation flow at high flow rates and large-scale flow inhomogeneity, pressure drops in the BCC scaffolds no longer follow the Ergun equation at higher Re.

REFERENCES

Abueidda, Diab W, Bakir, Mete, Al-Rub, Rashid K Abu & Bergstr 2017 *Mater. Des.* **122**, 255–267.

Al-Ketan, Oraib & Abu Al-Rub, Rashid K 2019 Multifunctional mechanical metamaterials based on triply periodic minimal surface lattices. *Advanced Engineering Materials* **21** (10), 1900524.

Bobbert, FSL, Lietaert, K, Eftekhari, Ali Akbar, Pouran, Behdad & Ahmadi 2017 *Acta Biomater.* **53**, 572–584.

Brakke, Kenneth A 1992 The surface evolver. *Experimental mathematics* **1** (2), 141–165.

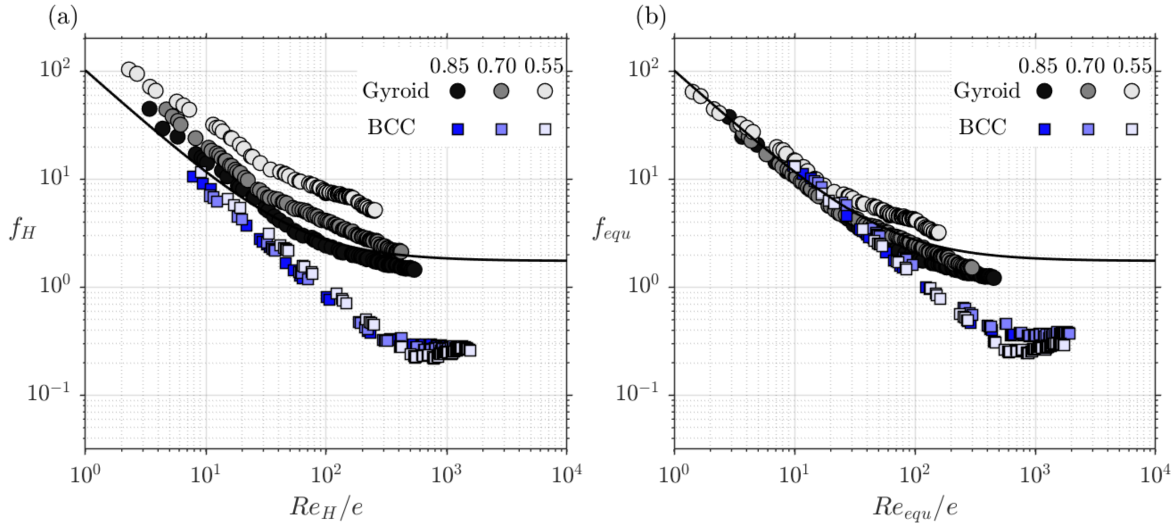

Figure 3. (a) Nondimensional pressure gradients of the gyroids and BCC scaffolds at three different porosities. (b) Nondimentional pressure gradients are replotted with equivalent hydraulic diameters, d_{equ}.

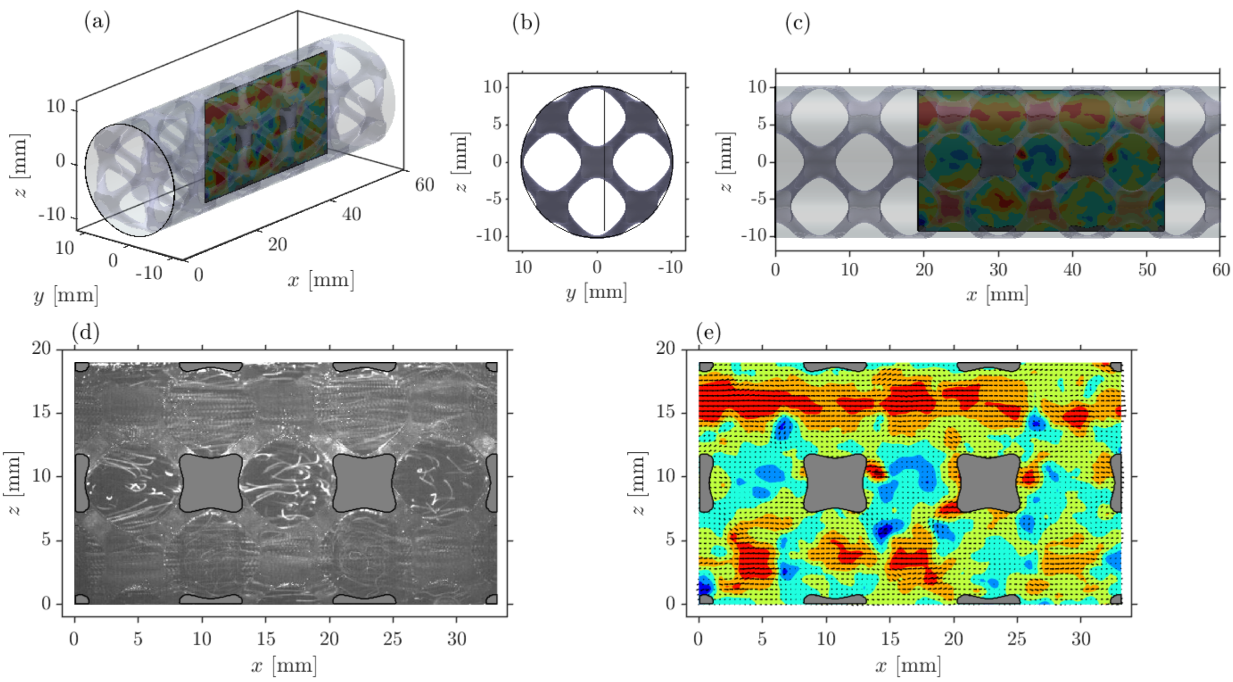

Figure 4. (a) Isometric view of the last BCC scaffold at the porosity of 0.85 in the measurment section. (b) Side view of (a). Solid vertical line represents a laser plane passing through 1 mm away from the center. (c) Front view of (a). (d) Overlay of consecutive 55 images to visualize the fluid flow with the masking image. (e) Velocity field (red-high, and blue-low)in the x-direction with the masking image. Grey regions represent solid parts where the laser plane pass through. The middle gray regions are nodes at the center in (b).

Castro, A. P. G., Pires, T., Santos, J. E., Gouveia, B. P. & Fernandes, P. R. 2019 *Materials* **12** (8), 1313.

Ergun, S. & Orning, A. A. 1949 *Ind. Eng. Chem.* **41** (6), 1179–1184.

Karcher, Hermann 1988 Embedded minimal surfaces derived from scherk's examples. *Manuscripta mathematica* **62** (1), 83–114.

Nitsche, Johannes C 1989 *Lectures on minimal surfaces: vol. 1*. Cambridge university press.

Vijayavenkataraman, Sanjairaj, Zhang, Lei, Zhang, Shuo, Hsi Fuh, Jerry Ying & Lu, Wen Feng 2018 Triply periodic minimal surfaces sheet scaffolds for tissue engineering applications: An optimization approach toward biomimetic scaffold design. *ACS Applied Bio Materials* **1** (2), 259–269.

Von Schnering, HG & Nesper, R 1991 Nodal surfaces of fourier series: fundamental invariants of structured matter. *Zeitschrift für Physik B Condensed Matter* **83** (3), 407–412.

Wood, Brian D, He, Xiaoliang & Apte, Sourabh V 2020 *Annu. Rev. Fluid Mech.* **52**, 171–203.

Zhao, Miao, Liu, Fei, Fu, Guang, Zhang, David Z, Zhang, Tao & Zhou, Hailun 2018 *Materials* **11** (12), 2411.